Vilniaus universitetas

Fizikos fakultetas

Cheminės fizikos institutas

Agnius Žukas

VANDENYJE TIRPAUS CHLOROFILŲ KOMPLEKSO (WSCP) NETIESINIŲ SPEKTRŲ MODELIAVIMAS

MAGISTRANTŪROS STUDIJŲ BAIGIAMASIS DARBAS

Teorinės fizikos ir astrofizikos studijų programa

Studentas   Agnius Žukas

Leista ginti

Darbo vadovas   prof. dr. Darius Abramavičius

Konsultantas   Mantas Jakučionis

Instituto direktorius   prof. dr. Darius Abramavičius

Vilnius 2023

Vilnius university

Faculty of physics

Institute of Chemical Physics

Agnius Žukas

MODELING NONLINEAR SPECTRA OF WATER SOLUBLE CHLOROPHYLL-BINDING PROTEIN (WSCP)

MASTER'S STUDIES FINAL THESIS

Theoretical Physics and Astrophysics study program

Student   Agnius Žukas

Allowed to defend

Academic supervisor   prof. dr. Darius Abramavičius

Consultant   Mantas Jakučionis

Director of the Institute   prof. dr. Darius Abramavičius

Vilnius 2023

Contents

1 Introduction

Light harvesting molecular aggregates, such as pigment-protein complexes, are fundamental components of photosynthetic apparatus, utilized by plants, algae, and some bacteria to convert sunlight into chemical energy. Understanding the structure, function, and excitation quantum dynamics in these molecular complexes is crucial to unravel the fundamental principles of solar energy conversion in Nature and for developing efficient synthetic solar cells. During photosynthesis, these complexes collect sunlight energy in specialized light-harvesting antennas and supply energy to the "reaction centers", where the excitation energy is used to separate the charges. Chlorophylls are the basic pigments that can be found in numerous structures. One of the most essential photosynthetic aggregates is the water-soluble chlorophyll-binding protein (WSCP), which is a ubiquitous molecular complex found in various photosynthetic organisms, including cyanobacteria, algae, and higher plants [1, 2]. Although WSCPs do not directly participate in photosynthesis, their small number of tightly packed pigments in a hydrophobic cavity at the center of the complex make them an ideal model system for studying pigment-pigment and pigment-protein interactions and are of great interest for high-resolution spectroscopic and modeling studies [3,4]. WSCPs can be categorized into two classes based on their ability to photoconvert: class I proteins can alter the absorption spectrum of the chromophores when exposed to light, while class II proteins do not possess this function [1]. Class II WSCPs include two subclasses, IIa (e.g. from Brassica oleracea var. Botrys) and IIb (e.g. from Lepidium (L.) virginicum). Our focus is on the latter subclass, which consists of four chlorophylls (Chls) in a tetramer and acts as two weakly coupled dimers [5,6]. The aggregate is made up of four proteins surrounding a hydrophobic core in the center. Within this core, four chlorophyll pigment molecules, either Chl-a or Chl-b, can be embedded. The model of WSCP that we will be using contains four identical Chl-b pigment molecules.

Systems like WSCP, exhibit complex excitation quantum dynamics and are usually modeled using the Frenkel exciton model coupled to harmonic vibrational modes, representing the quantum system and its environment. A number of methods have been developed to describe quantum dynamics and one such method, which we will be applying here, is the Time-Dependent Dirac–Frenkel Variational Principle. This method is used in quantum mechanics to calculate the time-evolution of a quantum system based on the chosen trial wavefunction. Usually, trial wavefunction is one of the Davydov ansatze, which is a group of wavefunctions that utilize Gaussian wavepackets, also known as coherent states, to represent vibronic states of molecular aggregates [7]. In reality, wavepackets are not as simple as the Gaussians, and the relationship between electrons and vibrations is often non-linear [8,9]. Additionally, the accuracy of the method is also heavily dependent on the choice of the trial wavefunction. A highly effective strategy is to employ the multi-Davydov D2 ansatz, which involves combining several D2 ansatze to expand the parameter space and enhance the accuracy of the vibrational mode representation [8, 10]. A different approach is to substitute the coherent state $|\tilde{\lambda}\rangle = \hat{D}(\lambda)|0\rangle$ with squeezed coherent states $|\lambda, \zeta\rangle = \hat{D}(\lambda)\hat{S}(\zeta)|0\rangle$, which have extra degrees of freedom (DOFs) that enable the wavepacket to contract and expand in its phase space along both coordinate and momentum axes. Here displacement and squeezing operators are expressed as [7]

$$\hat{D}_i(\lambda_i) = \exp\left(\lambda_i \hat{b}_i^\dagger - \lambda_i^* \hat{b}_i\right), \tag{1}$$

$$\hat{S}_i(\zeta_i) = \exp\left(\frac{1}{2}\left(\zeta_i^* \hat{b}_i^2 - \zeta_i \hat{b}_i^{\dagger 2}\right)\right), \tag{2}$$

with λ_i and ζ_i representing displacement parameter and complex squeeze parameter respectively. Furthermore, the squeezing parameter is expressed in polar form $\zeta_i = r_i e^{i\theta_i}$, where r_i is squeezing amplitude and θ_i is squeezing angle. With squeezed coherent state we are able to deform Gaussian wavepacket as shown in Fig. (1). First starting by circular disc of the ordinary vacuum state centered on the origin, second step is squeezing and rotating into the elliptical disc by applying $\hat{S}(\zeta)$ operator, the final third step is to shift the elliptical disc by applying $\hat{D}(\lambda)$ operator.
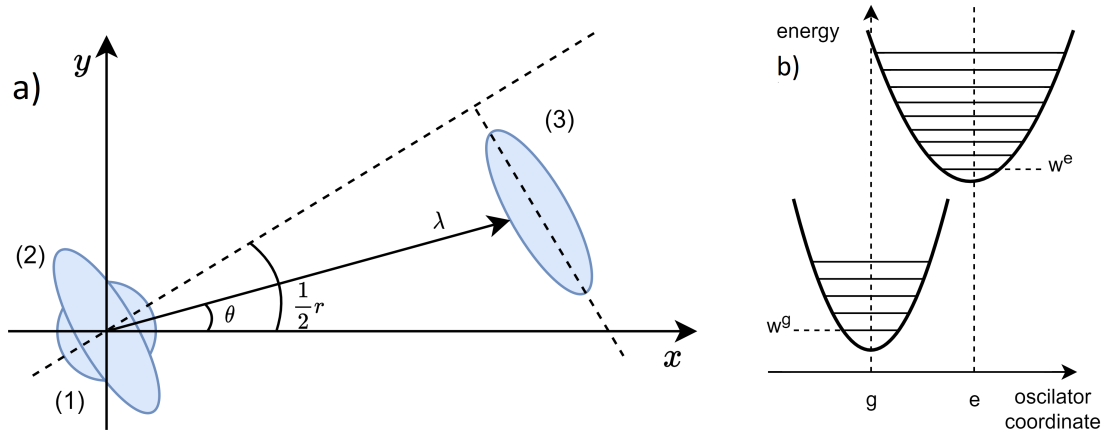
1 Fig. (a) Phase space plot squeezed coherent state [7]: (1) The ordinary vacuum state, (2) the squeezed vacuum state, and (3) the squeezed coherent state. (b) Squeezed oscillator energy diagram, note how an excited state energy potential becomes shallower which in turn shifts each vibrational mode energy level.

To comprehensively investigate the excitation dynamics in photosynthetic pigment-proteins aggregates, a diverse range of spectroscopic methods can be employed experimentally. One of the simplest and most widely used is linear absorption spectroscopy [11]. The absorption spectra can provide valuable information about excitation energies and other photophysical properties. A more advanced technique called two-dimensional electronic spectroscopy (2DES) [11] was developed relatively recently and has become an essential tool for studying various systems in physics, chemistry, and biology [12]. 2DES provides several benefits over traditional one-dimensional spectroscopy, such as additional temporal resolution, enhanced signal-to-noise ratio, and the capability to distinguish overlapping transitions, among others [13].

Therefore the objective of this work is to employ the squeezed coherent state vibronic wavepacket in the TDVP approach to investigate electronic and vibrational excitations, to introduce quadratic coupling into the 3-band model and finally, to compare the calculated WSCP linear absorption and 2DES spectra with previously published experimental WSCP spectra.

2 Theory

When an external laser pulse is applied to an aggregate, it excites not a single pigment molecule, but rather multiple sites of the entire aggregate simultaneously, resulting in the creation coherent superposition of molecular excitations, which is called an exciton [14]. The exciton behaves as a single quasiparticle with its own characteristic energy and momentum, and it can transfer energy through the group of molecules. Organic molecules usually exhibit tightly localized molecular orbitals around the individual molecules therefore a specific type of exciton is used, called Frenkel exciton. The excitations are bound to interact with surrounding vibrations, hence it is assumed that our system possesses two types of vibrational degree of freedom, namely intramolecular pigment vibrational modes, and vibrational modes of the surrounding protein, often denoted as phonons. All vibrational modes are represented by quantum harmonic oscillators. Henceforth, we will be referring to pigment molecules as sites and proteins as baths. Putting together every degree of freedom and interaction, we get a total system Hamiltonian as

$$\hat{H} = \hat{H}_{\text{S}} + \left(\hat{H}_{\text{B}} + \hat{H}_{\text{S-B}} \right) + \left(\hat{H}_{\text{V}} + \hat{H}_{\text{S-V}} \right) + \hat{H}_{\text{nonlinear}}, \tag{3}$$

where $\hat{H}_{\text{S}}$ represents site single-excitation Hamiltonian, $\hat{H}_{\text{B}}$ - bath vibrational Hamiltonian, $\hat{H}_{\text{S-B}}$ - site and bath interaction Hamiltonian, $\hat{H}_{\text{V}}$ is intramolecular pigment vibrational Hamiltonian, $\hat{H}_{\text{S-V}}$ is site and intramolecular vibration interaction Hamiltonian and final $\hat{H}_{\text{nonlinear}}$ denotes the quadratic coupling between site and bath vibrations. Fig. (2) displays a schematic view of the system under investigation. All of the above is explicitly expressed as

$$\hat{H}_{\text{S}} = \sum_{n} \varepsilon_n \hat{a}_n^{\dagger} \hat{a}_n + \sum_{n,m}^{n \neq m} V_{nm} \hat{a}_n^{\dagger} \hat{a}_m, \tag{4}$$

$$\hat{H}_{\text{B}} = \sum_{n,p} \omega_{np}^{g} \hat{b}_{np}^{\dagger} \hat{b}_{np}, \tag{5}$$

$$\hat{H}_{\text{S-B}} = - \sum_{n} \hat{a}_n^{\dagger} \hat{a}_n \sum_{p} \omega_{np}^{e} g_{np} \left(\hat{b}_{np}^{\dagger} + \hat{b}_{np} \right), \tag{6}$$

$$\hat{H}_{\text{V}} = \sum_{n,q} w_{nq} \hat{c}_{nq}^{\dagger} \hat{c}_{nq}, \tag{7}$$

$$\hat{H}_{\text{S-V}} = - \sum_{n} \hat{a}_n^{\dagger} \hat{a}_n \sum_{q} w_{nq} f_{nq} \left(\hat{c}_{nq}^{\dagger} + \hat{c}_{nq} \right), \tag{8}$$

$$\hat{H}_{\text{nonlinear}} = \sum_{n} \hat{a}_n^{\dagger} \hat{a}_n \sum_{p} \frac{\left(\omega_{np}^{e} - \omega_{np}^{g} \right)}{4} \left(\hat{b}_{np}^{\dagger} + \hat{b}_{np} \right)^2, \tag{9}$$

where ε_n denotes nth site electronic excitation energy, V_{nm} is the resonant coupling between the nth and mth site. $\hat{a}_n^{\dagger}$ and $\hat{a}_n$ are the creation and annihilation operators for electronic excitation of site, while $\hat{b}_{np}^{\dagger}$ and $\hat{b}_{np}$ are bosonic creation and annihilation operators for pth bath vibrational mode. Similarly, $\hat{c}_{nq}^{\dagger}$ and $\hat{c}_{nq}$ are creation and annihilation operators for qth intramolecular vibration mode. Furthermore, each bath vibrational mode is described by two frequencies in ground state

ω_{np}^g and excited state ω_{np}^e together with dimensionless linear coupling strength g_{np}. While each intramolecular vibrational mode is described by a single frequency w_{nq} with coupling strength f_{nq}. The last Hamiltonian term represented by $\hat{H}_{\text{nonlinear}}$ accounts for nonlinearity in our model and it becomes relevant once the vibrational mode frequencies in the electronic ground state are different from the ones in the excited state as shown in Fig. (3). Otherwise this term does not contribute to the total Hamiltonian. The quadratic coupling term arises from the difference of mode frequency in ground and excited states and is proportional to the square of the vibrational displacement. This effect can play a significant role in determining the optical properties and dynamics of pigment-protein complexes and other quantum systems.
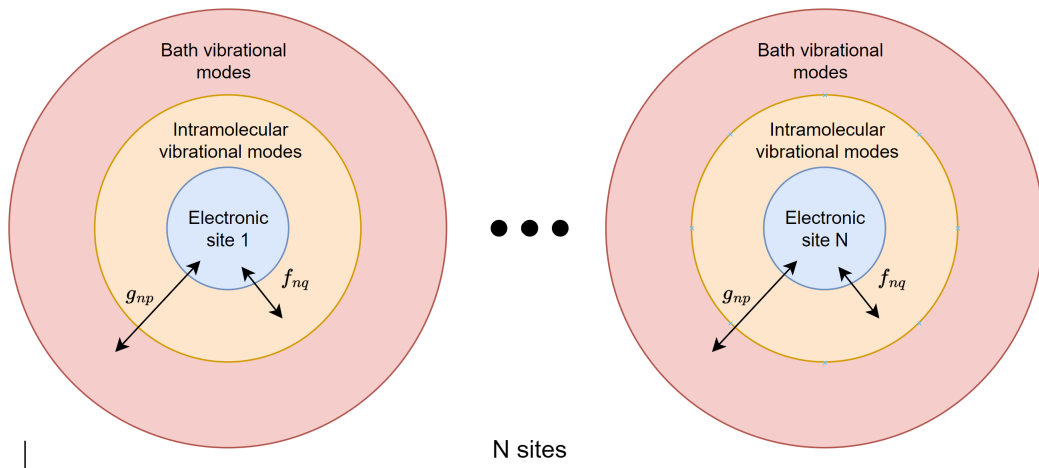
2 Fig. Diagram representation of the system model under investigation. Blue circles denote a single site or a pigment, orange circle denote intramolecular pigment vibrational modes and red circle denote bath or protein vibrational modes. While arrows indicate coupling between electronic site and intramolecular pigment vibrational modes f_{nq}, and coupling between electronic site and bath vibrational modes g_{np}.
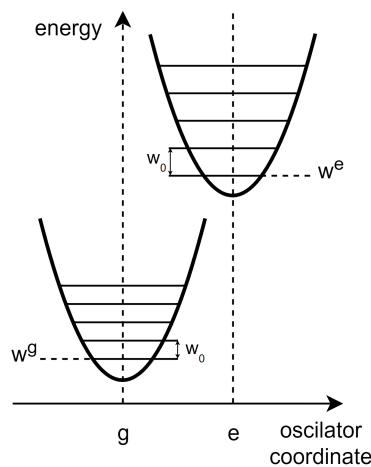
3 Fig. Harmonic oscillator model energy diagram. Shown here how the frequency gap ω_0 is different for the ground and excited states. This also means that $\omega^e - \omega^g \neq 0$.

2.1 Time-dependent Dirac–Frenkel variational principle

To obtain our system model excitation dynamics we will be using Time-dependent Dirac–Frenkel variational principle (TDVP). The performed various simulations [15–18] show that this technique is a powerful and flexible tool for simulating the relaxation dynamics of a quantum system. The approach involves a certain trial wavefunction that is expressed as a linear combination of time-dependent basis functions, with the aim of minimizing the quantum action functional expressed as

$$S = \int_0^t \mathcal{L} dt, \tag{10}$$

where S denotes the action functional and $\mathcal{L}$ represents the Lagrangian function, or just the Lagrangian. When using the Hamiltonian and the trial wavefunction, the Lagrangian is written as

$$\mathcal{L} = \frac{i}{2} \left(\langle \Psi | \dot{\Psi} \rangle - \langle \dot{\Psi} | \Psi \rangle \right) - \langle \Psi | \hat{H} | \Psi \rangle, \tag{11}$$

where we set $\hbar = 1$ for simplicity. The trial wavefunction produces deviation from the solution of the Schrödinger equation and we aim to minimize this deviation to make our trial wavefunction as close as possible to the exact wavefunction of the system. With this procedure, we will obtain a set of differential equations of motion for parameters $\{\alpha, \lambda, \tilde{\lambda}, \theta, r\}$ which can be used to simulate the coupled dynamics. To accomplish this, we can employ the Euler-Lagrange equations to derive equations of motion for each of the aforementioned parameters

$$\frac{d}{dt} \left(\frac{\partial \mathcal{L}}{\partial \dot{f}_i^*} \right) - \frac{\partial \mathcal{L}}{\partial f_i^*} = 0, \tag{12}$$

here f represents an arbitrary parameter.

TDVP accuracy highly depends on the wavefunction in use, the more precise the wavefunction, the more precise results we get. In this work we will be using the same D2 ansatz but with a slight variation, where instead of vibrational coherent state we will be using squeezed coherent state. We also assume that the collective electronic excitations in a molecular aggregate can be described as a sum of three band system. The primary state of the system is the electronic ground state g, when the electronic subsystem is not excited, only vibrations can be in non-equilibrium state and expressed as

$$|\Psi\rangle_g = e^{i\beta} \prod_{k,q} |\lambda, \zeta\rangle_{kq} \prod_{h,q} |\tilde{\lambda}\rangle_{hq}, \tag{13}$$

where β is the phase factor, $|\lambda, \zeta\rangle_{kq}$ represents bath vibrational squeezed coherent state and $|\tilde{\lambda}\rangle_{hq}$ represents intramolecular vibrational coherent state. Next is the single excited state e, corresponding to a case where only one site is electronically excited in the aggregate described by

$$|\Psi\rangle_e = \sum_n \alpha_n |n\rangle_{el} \prod_{k,q} |\lambda, \zeta\rangle_{kq} \prod_{h,q} |\tilde{\lambda}\rangle_{hq}, \tag{14}$$

where α_n is the site excitation amplitude and $|n\rangle_{el}$ denotes the electronic excitation for site n. For

2DES calculations it is important to include double excited state f. It corresponds to a case where any two sites are electronically excited in the aggregate and expressed as

$$|\Psi\rangle_f = \sum_{[n,m]}^{n \leq m} \alpha_{[n,m]} |n,m\rangle_{el} \prod_{k,q} |\lambda, \zeta\rangle_{kq} \prod_{h,q} |\tilde{\lambda}\rangle_{hq}, \tag{15}$$

where n and m indices represent distinct sites.

The primary emphasis of this study was placed on deriving and rearranging complex equations. As a starting point, we derived the Lagrangian for the g state, which is expressed as

$$\begin{aligned}
\mathcal{L} = & \frac{i}{2} \sum_{k,q} \left(\dot{\lambda}_{kq} \lambda_{kq}^* - \dot{\lambda}_{kq}^* \lambda_{kq} + i\dot{\theta}_{kq} \sinh^2\left(r_{kq}\right) \right) \\
& + \frac{i}{2} \sum_{d,f} \left(\dot{\tilde{\lambda}}_{df} \tilde{\lambda}_{df}^* - \dot{\tilde{\lambda}}_{df}^* \tilde{\lambda}_{df} \right) \\
& - \sum_{k,q} \omega_{kq}^g \left(\sinh^2\left(r_{kq}\right) + \lambda_{kq}^* \lambda_{kq} \right) \\
& - \sum_{i,q} w_{iq} \tilde{\lambda}_{iq}^* \tilde{\lambda}_{iq}.
\end{aligned} \tag{16}$$

Then, using the Euler-Lagrange equation Eq. (12) we got at a corresponding set of first-order differential equations

$$\dot{\alpha}_n = 0, \tag{17}$$

$$\dot{\lambda}_{kq} = -i\omega_{kq}^g \lambda_{kq}, \tag{18}$$

$$\dot{\tilde{\lambda}}_{kh} = -iw_{kh} \tilde{\lambda}_{kh}, \tag{19}$$

$$\dot{r}_{uv} = 0, \tag{20}$$

$$\dot{\theta}_{\mu v} = -2\omega_{\mu v}^g. \tag{21}$$

For the e state we derived Lagrangian as

$$\mathcal{L} = \frac{i}{2} \sum_n \alpha_n^* \dot{\alpha}_n - \frac{i}{2} \sum_n \alpha_n \dot{\alpha}_n^*$$

$$+ \frac{i}{2} \sum_n |\alpha_n|^2 \sum_{k,q} \left(\dot{\lambda}_{kq} \lambda_{kq}^* - \dot{\lambda}_{kq}^* \lambda_{kq} + i\dot{\theta}_{kq} \sinh^2 (r_{kq}) \right)$$

$$+ \frac{i}{2} \sum_n |\alpha_n|^2 \sum_{d,f} \left(\dot{\tilde{\lambda}}_{df} \tilde{\lambda}_{df}^* - \dot{\tilde{\lambda}}_{df}^* \tilde{\lambda}_{df} \right)$$

$$- \sum_n \alpha_n^* \alpha_n \varepsilon_n - \sum_{n,m}^{n \neq m} V_{nm} \alpha_m \alpha_n^*$$

$$- \sum_n |\alpha_n|^2 \sum_{k,q} \omega_{kq}^g \left(\sinh^2 (r_{kq}) + \lambda_{kq}^* \lambda_{kq} \right)$$

$$+ \sum_n |\alpha_n|^2 \sum_q \omega_{nq}^e g_{nq} \left(\lambda_{nq} + \lambda_{nq}^* \right)$$

$$- \sum_n |\alpha_n|^2 \sum_{i,q} w_{iq} \tilde{\lambda}_{iq}^* \tilde{\lambda}_{iq}$$

$$+ \sum_n |\alpha_n|^2 \sum_q w_{nq} f_{nq} \left(\tilde{\lambda}_{nq} + \tilde{\lambda}_{nq}^* \right)$$

$$- \sum_n |\alpha_n|^2 \sum_k \left(\omega_{nk}^e - \omega_{nk}^g \right) \left(\cosh (2r_{nk}) - \sinh (2r_{nk}) \cos (\theta_{nk}) + \left(\lambda_{nk} + \lambda_{nk}^* \right)^2 \right). \qquad (22)$$

And got a corresponding set of differential equations expressed as

$$\dot{\alpha}_n = -\frac{i}{\rho} \alpha_n \sum_{k,q} |\alpha_k|^2 \omega_{kq}^e g_{kq} \mathrm{Re}\lambda_{kq} - \frac{i}{\rho} \alpha_n \sum_{h,q} |\alpha_h|^2 w_{hq} f_{hq} \mathrm{Re}\tilde{\lambda}_{hq}$$

$$+ \frac{i}{\rho} \alpha_n \sum_{k,q} |\alpha_k|^2 \Delta\omega_{kq} \left(2\mathrm{Re}\lambda_{kq} \right)^2$$

$$+ \frac{i}{\rho} 2\alpha_n \sum_{k,q} |\alpha_k|^2 \Delta\omega_{kq} \left(1 - \coth (2r_{kq}) \cos (\theta_{kq}) \right) \sinh^2 (r_{kq})$$

$$- i\alpha_n \varepsilon_n - i \sum_m^{n \neq m} V_m \alpha_m$$

$$+ i2\alpha_n \sum_q \omega_{nq}^e g_{nq} \mathrm{Re}\lambda_{nq} + i2\alpha_n \sum_q w_{nq} f_{nq} \mathrm{Re}\tilde{\lambda}_{nq}$$

$$- i\alpha_n \sum_q \Delta\omega_{nq} \left(\cosh (2r_{nq}) - \sinh (2r_{nq}) \cos (\theta_{nq}) + \left(2\mathrm{Re}\lambda_{nq} \right)^2 \right), \qquad (23)$$

$$\dot{\lambda}_{kq} = -i\omega_{kq}^g \lambda_{kq} + i\frac{1}{\rho} |\alpha_k|^2 \omega_{kq}^e g_{kq} - 4\frac{i}{\rho} |\alpha_k|^2 \Delta w_{kq} \mathrm{Re}\lambda_{kq}, \qquad (24)$$

$$\dot{\tilde{\lambda}}_{kh} = -iw_{kh} \tilde{\lambda}_{kh} + \frac{i}{\rho} |\alpha_k|^2 w_{kh} f_{kh}, \qquad (25)$$

9

$$\dot{r}_{uv} = \frac{2}{\rho}|\alpha_u|^2 \Delta\omega_{uv} \sin\left(\theta_{uv}\right), \tag{26}$$

$$\dot{\theta}_{\mu v} = -2\omega_{\mu v}^g - \frac{4}{\rho}|\alpha_\mu|^2 \Delta\omega_{\mu v}\left(1 - \coth\left(2r_{\mu v}\right)\cos\left(\theta_{\mu v}\right)\right), \tag{27}$$

where we denoted vibrational mode frequency difference as $\Delta\omega = \omega^e - \omega^g$ and $\rho = \sum_n \alpha_n^* \alpha_n$. And for the final state f, we derived Lagrangian as

$$
\begin{aligned}
\mathcal{L} = {} & \frac{\mathrm{i}}{2}\sum_{[n,m]}^{n\leq m} \alpha_{[n,m]}^* \dot{\alpha}_{[n,m]} - \frac{\mathrm{i}}{2}\sum_{[n,m]}^{n\leq m} \alpha_{[n,m]} \dot{\alpha}_{[n,m]}^* \\
& + \frac{\mathrm{i}}{2}\sum_{[n,m]}^{n\leq m} |\alpha_{[n,m]}|^2 \sum_{k,q}\left(\dot{\lambda}_{kq}\lambda_{kq}^* - \dot{\lambda}_{kq}^*\lambda_{kq} + \mathrm{i}\dot{\theta}_{kq}\sinh^2\left(r_{kq}\right)\right) \\
& + \frac{\mathrm{i}}{2}\sum_{[n,m]}^{n\leq m} |\alpha_{[n,m]}|^2 \sum_{d,f}\left(\dot{\tilde{\lambda}}_{df}\tilde{\lambda}_{df}^* - \dot{\tilde{\lambda}}_{df}^*\tilde{\lambda}_{df}\right) \\
& - \sum_{[a,b]}^{a\leq b}\sum_{[n,m]}^{n\leq m} \alpha_{[a,b]}^*\alpha_{[n,m]}\left(\sum_i \varepsilon_i \mathcal{N}_{i,[n,m]}^{i,[a,b]} + \sum_{i,j}^{i\neq j} V_{ij}\mathcal{N}_{j,[n,m]}^{i,[a,b]}\right) \\
& - \sum_{[n,m]}^{n\leq m} |\alpha_{[n,m]}|^2 \sum_{k,q}\omega_{kq}^g\left(\sinh^2\left(r_{kq}\right) + \lambda_{kq}^*\lambda_{kq}\right) \\
& + \sum_{[a,b]}^{a\leq b}\sum_{[n,m]}^{n\leq m} \alpha_{[a,b]}^*\alpha_{[n,m]}\sum_i \mathcal{N}_{i,[n,m]}^{i,[a,b]}\sum_k \omega_k^e g_{ik}\left(\lambda_{ik} + \lambda_{ik}^*\right) \\
& - \sum_{[n,m]}^{n\leq m} |\alpha_{[n,m]}|^2 \sum_{i,q}w_{iq}\tilde{\lambda}_{iq}^*\tilde{\lambda}_{iq} \\
& + \sum_{[a,b]}^{a\leq b}\sum_{[n,m]}^{n\leq m} \alpha_{[\alpha,\beta]}^*\alpha_{[n,m]}\sum_i \mathcal{N}_{i,[n,m]}^{i,[\alpha,\beta]}\sum_q w_{iq}f_{iq}\left(\tilde{\lambda}_{iq} + \tilde{\lambda}_{iq}^*\right) \\
& - \sum_{[a,b]}^{a\leq b}\sum_{[n,m]}^{n\leq m} \alpha_{[a,b]}^*\alpha_{[n,m]}\sum_i \mathcal{N}_{i,[n,m]}^{i,[a,b]}\sum_k \left(\omega_{ik}^e - \omega_{ik}^g\right)\left(\cosh\left(2r_{ik}\right) - \sinh\left(2r_{ik}\right)\cos\left(\theta_{ik}\right) + \left(\lambda_{ik} + \lambda_{ik}^*\right)^2\right),
\end{aligned}
$$
$$\tag{28}$$

where

$$\mathcal{N}_{[n,m]}^{[\alpha,\beta]} = \langle\alpha,\beta|_{el}|n,m\rangle_{el}, \tag{29}$$

$$\mathcal{N}_{j,[n,m]}^{i,[\alpha,\beta]} = \langle\alpha,\beta|_{el}\hat{a}_i^\dagger\hat{a}_j|n,m\rangle_{el}, \tag{30}$$

$$\mathcal{N}_{v\mu,[n,m]}^{v\mu,[\alpha,\beta]} = \langle\alpha,\beta|_{el}\hat{a}_v^\dagger\hat{a}_\mu^\dagger\hat{a}_v\hat{a}_\mu|n,m\rangle_{el}. \tag{31}$$

The corresponding set of differential equations were derived as

$$
\begin{aligned}
\dot{\alpha}_{[n,m]} = & -\frac{\mathrm{i}}{\rho}\alpha_{[n,m]}\sum_{k,q}\sum_{[a,b]}^{a\leq b}\sum_{[x,y]}^{x\leq y}\alpha_{[a,b]}^{*}\alpha_{[x,y]}\mathcal{N}_{k,[x,y]}^{k,[a,b]}\omega_{kq}^{e}g_{kq}\mathrm{Re}\lambda_{kq} \\
& -\frac{\mathrm{i}}{\rho}\alpha_{[n,m]}\sum_{h,q}\sum_{[a,b]}^{a\leq b}\sum_{[x,y]}^{x\leq y}\alpha_{[a,b]}^{*}\alpha_{[x,y]}\mathcal{N}_{h,[x,y]}^{h,[a,b]}w_{hq}f_{hq}\mathrm{Re}\tilde{\lambda}_{hq} \\
& +\frac{\mathrm{i}}{\rho}\alpha_{[n,m]}\sum_{k,q}\sum_{[a,b]}^{a\leq b}\sum_{[x,y]}^{x\leq y}\alpha_{[a,b]}^{*}\alpha_{[x,y]}\mathcal{N}_{k,[x,y]}^{k,[a,b]}\Delta\omega_{kq}\left(2\mathrm{Re}\lambda_{kq}\right)^{2} \\
& +\frac{\mathrm{i}}{\rho}2\alpha_{[n,m]}\sum_{k,q}\sum_{[a,b]}^{a\leq b}\sum_{[x,y]}^{x\leq y}\alpha_{[a,b]}^{*}\alpha_{[x,y]}\mathcal{N}_{k,[x,y]}^{k,[a,b]}\Delta\omega_{kq}\left(1-\coth\left(2r_{kq}\right)\cos\left(\theta_{kq}\right)\right)\sinh^{2}\left(r_{kq}\right) \\
& -\mathrm{i}\sum_{[a,b]}^{a\leq b}\alpha_{[a,b]}\sum_{i}\varepsilon_{i}\mathcal{N}_{i,[n,m]}^{i,[a,b]} \\
& -\mathrm{i}\sum_{[a,b]}^{a\leq b}\alpha_{[a,b]}\sum_{i,j}^{i\neq j}V_{ij}\mathcal{N}_{j,[n,m]}^{i,[a,b]} \\
& +\mathrm{i}2\sum_{[a,b]}^{a\leq b}\alpha_{[a,b]}\sum_{i}\mathcal{N}_{i,[n,m]}^{i,[a,b]}\sum_{q}\omega_{kq}^{e}g_{kq}\mathrm{Re}\lambda_{kq} \\
& +\mathrm{i}2\sum_{[a,b]}^{a\leq b}\alpha_{[a,b]}\sum_{i}\mathcal{N}_{i,[n,m]}^{i,[a,b]}\sum_{q}w_{iq}f_{iq}\mathrm{Re}\tilde{\lambda}_{iq} \\
& -\mathrm{i}\sum_{[a,b]}^{a\leq b}\alpha_{[a,b]}\sum_{i}\mathcal{N}_{i,[n,m]}^{i,[a,b]}\sum_{q}\Delta\omega_{iq}\left(\cosh\left(2r_{iq}\right)-\sinh\left(2r_{iq}\right)\cos\left(\theta_{iq}\right)+\left(2\mathrm{Re}\lambda_{iq}\right)^{2}\right),
\end{aligned}
\tag{32}
$$

$$
\begin{aligned}
\dot{\lambda}_{kq} = & -\mathrm{i}\omega_{kq}^{g}\lambda_{kq}+\mathrm{i}\frac{1}{\rho}\sum_{[a,b]}^{a\leq b}\sum_{[n,m]}^{n\leq m}\alpha_{[a,b]}^{*}\alpha_{[n,m]}\mathcal{N}_{k,[n,m]}^{k,[a,b]}\omega_{kq}^{e}g_{kq} \\
& -4\frac{\mathrm{i}}{\rho}\sum_{[a,b]}^{a\leq b}\sum_{[n,m]}^{n\leq m}\alpha_{[a,b]}^{*}\alpha_{[n,m]}\mathcal{N}_{k,[n,m]}^{k,[a,b]}\Delta w_{kq}\mathrm{Re}\lambda_{kq},
\end{aligned}
\tag{33}
$$

$$
\dot{\tilde{\lambda}}_{kh} = -\mathrm{i}w_{kh}\tilde{\lambda}_{kh}+\frac{\mathrm{i}}{\rho}\sum_{[a,b]}^{a\leq b}\sum_{[n,m]}^{n\leq m}\alpha_{[a,b]}^{*}\alpha_{[n,m]}\mathcal{N}_{k,[n,m]}^{k,[a,b]}w_{kh}f_{kh},
\tag{34}
$$

$$
\dot{r}_{uv} = \frac{2}{\rho}\sum_{[a,b]}^{a\leq b}\sum_{[n,m]}^{n\leq m}\alpha_{[a,b]}^{*}\alpha_{[n,m]}\mathcal{N}_{u,[n,m]}^{u,[a,b]}\Delta\omega_{uv}\sin\left(\theta_{uv}\right),
\tag{35}
$$

$$
\dot{\theta}_{\mu v} = -2\omega_{\mu v}^{g}-\frac{4}{\rho}\sum_{[a,b]}^{a\leq b}\sum_{[n,m]}^{n\leq m}\alpha_{[a,b]}^{*}\alpha_{[n,m]}\mathcal{N}_{\mu,[n,m]}^{\mu,[a,b]}\Delta\omega_{\mu v}\left(1-\coth\left(2r_{\mu v}\right)\cos\left(\theta_{\mu v}\right)\right),
\tag{36}
$$

One interesting point to make here is that only the last two terms r_{ab} and θ_{uv}, which compose the squeezing parameter $\zeta = re^{i\theta}$, depend on $\Delta\omega$. Now if we look back to our model Hamiltonian terms Eq. (4-9), we instantly see that only the nonlinear interaction term includes this difference between two frequencies. This means that only by including nonlinear interaction we can generate squeezing, otherwise if $\Delta\omega = 0$, the equation of motion for the squeezing amplitude also becomes zero and squeezing angle becomes constant in time.

2.2   Absorption spectrum

The first observable that we will be investigating is the absorption spectrum. For that, we can use a simpler form of our model system with only two bands, namely ground g and single excited e states, which in turn allows us to use simpler equations of motion Eq. (23-23). To calculate the absorption spectrum, we assume that the system is excited with an optical field. The absorption spectrum can be obtained from the linear response theory by calculating a Fourier transform of the linear response function [19]

$$A(\omega) = \text{Re} \int_0^\infty dt e^{i\omega t} R^{abs}(t), \tag{37}$$

where $R(t)$ is the linear optical response function for a single realization and can be expressed as

$$R^{abs}(t) = \sum_{m,n} (\boldsymbol{\mu}_m \cdot \boldsymbol{o})(\boldsymbol{\mu}_n \cdot \boldsymbol{o}) \, \alpha_m^*(0) \, \alpha_n(t)$$
$$\times \langle \lambda_g(0), \zeta_g(0) | \lambda_e(t), \zeta_e(t) \rangle, \tag{38}$$

denoting $\boldsymbol{\mu}_n$ as the transition dipole moment vector for nth molecule, a $\boldsymbol{o}$ is randomly generated polarization vector of the electric field to simulate the orientational averaging. Subscripts g and e represent parameters in the ground and excited states respectively. The inner product of two distinct coherent states is [20]

$$\langle \lambda_g, \zeta_g | \lambda_e, \zeta_e \rangle = \frac{1}{\sqrt{\zeta}} \exp\left[-\frac{|\lambda_g|^2 + |\lambda_e|^2}{2} \right]$$
$$\times \exp\left[\frac{\lambda_g^* \lambda_e}{\zeta} \right]$$
$$\times \exp\left[\frac{\lambda_g^{*2}}{2\zeta} \left(e^{-i\theta_e} \cosh(r_g) \sinh(r_e) - e^{-i\theta_g} \cosh(r_e) \sinh(r_g) \right) \right]$$
$$\times \exp\left[\frac{\lambda_e^2}{2\zeta} \left(e^{i\theta_g} \cosh(r_e) \sinh(r_g) - e^{i\theta_e} \cosh(r_g) \sinh(r_e) \right) \right] \tag{39}$$
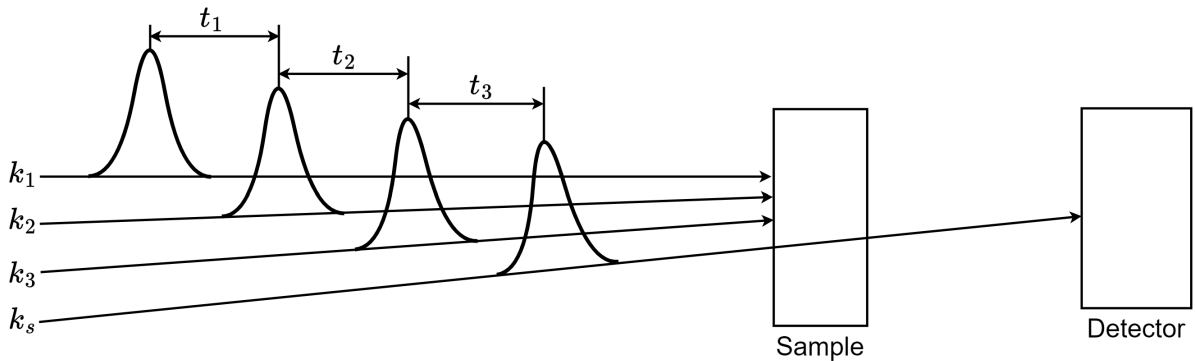
where

$$\zeta = \cosh(r_g) \cosh(r_e) - e^{i(\theta_e - \theta_g)} \sinh(r_g) \sinh(r_e) \tag{40}$$

12

2.3 Two-dimensional electronic spectroscopy (2DES)

Together with traditional one-dimensional spectroscopy, which measures the absorption of light as a function of just one variable, we also calculate and investigate two-dimensional electronic spectroscopy (2DES), which is able to use time and frequency resolution simultaneously. This relatively new technique provides us with the information about excited state relaxation dynamics of the complex system.

During the 2DES experiment a sample is excited with a sequence of two laser pulses separated by a time delay called the coherence time and denoted as t_1. After them a variable time delay, called the waiting time and is denoted as t_2, the weaker probe pulse is produced and then the resulting signal is recorded by a detector with a time delay called detection time and is denoted as t_3 [13]. A schematic representation of this setup is shown in Fig. (4). The optical pulses induce a third-order optical response function $S^{(3)}(t_1, t_2, t_3)$ in the excitonic system, from which is then possible to extract two-dimensional spectra as a function of excitation ω_1 and detection ω_3 frequencies by applying Furrier transform for t_1 and t_3 time delays [11, 19, 21]. Optical pulses are characterized by wavevectors $\vec{k}_1$, $\vec{k}_2$, $\vec{k}_3$. The signal $\vec{k}_s$ is a combination of these three vectors. Two types of signal are detected, one called rephasing (RP) with $\vec{k}_{RP} = -\vec{k}_1 + \vec{k}_2 + \vec{k}_3$ and non-rephasing (NRP) $\vec{k}_{NRP} = +\vec{k}_1 - \vec{k}_2 + \vec{k}_3$, and combining the RP and NRP signals yields a total 2DES spectrum.

4 Fig. Scheme of experimental setup used for 2DES.

This spectrum can exhibit a complicated network of peaks where the amplitude and shape of the peaks provide information about the strength and nature of the couplings between the electronic and vibrational degrees of freedom in the system, as well as the dynamics of the excitations. Peaks on the diagonal line of the spectrum correspond to emission at the same frequency as the excitation signal. Peaks located off the diagonal line in the 2D spectra, known as cross peaks, arise when the system emits a signal that oscillates at a different frequency than that of the excitation signal. The appearance of a cross peak suggests that the two resonances are coupled. The peaks discussed above can be associated with three distinct types of electronic transitions: excited state emission (ESE), ground state bleach (GSB), and excited state absorption (ESA). ESE happens when a molecule in an excited state goes through a transition from the excited states to a ground state. GSB takes place when a molecule in the ground state absorbs a photon and experiences a transition to an excited state, leading to a reduction or "bleaching" of the absorption at the corresponding ground-state energy.

ESA happens when a molecule in an excited state absorbs a photon and undergoes a transition to a higher excited state. Both ESE and GSB produce positive peaks representing an increase in signal intensity and are associated with absorption processes. While ESA produces negative peaks represent a decrease in the population of the excited state and a decrease in the detected signal intensity.

3 Results

3.1 Model parameters

To simulate WSCP dynamics, in our calculation we used experimentally measured [22] WSCP resonant coupling matrix values shown in Table (1) and transition dipole moment values presented in Table (2). In experiments, the sample being probed typically consists of multiple such aggregates, each of which can be resonantly excited by an external electric field, thus we set single site excitation energies to be $\varepsilon_n = \omega_{\text{field}}$, where ω_{field} is an external field frequency. Because of slow fluctuations in the whole sample, excitation energies shift in each aggregate randomly. To account for this, a static excitation energy disorder was also applied to the site excitation energies sampled from the Gaussian distribution with standard deviation at $\sigma = 70$ cm^{-1}, unless stated otherwise. Although this value was arbitrarily chosen, it falls within the same range as in other similar studies [21,23,24].

1 Table. WSCP resonant coupling matrix values between sites, cm^{-1}.

	1 site	2 site	3 site	4 site
1 site	/	67.51	5.21	15.02
2 site	67.51	/	14.86	5.68
3 site	5.21	14.86	/	66.60
4 site	15.02	5.68	66.60	/

2 Table. WSCP transition dipole moments.

	x	y	z
1 site	1.08	-1.26	3.45
2 site	2.58	-1.60	2.34
3 site	-1.02	2.13	-3.01
4 site	-2.52	0.89	-2.74

The TDVP method requires averaging over a number of stochastic realizations, and we found that 1000 realizations were sufficient to obtain converged results. Since WSCP consists of four identical pigment-protein pairs, and the vibrations of the protein molecules affect only the nearest pigment molecule, it can be said that the experimentally measured spectral density function is the same for each pair and corresponds to the logarithmic distribution function [23]. Spectral density function characterizes the frequency distribution of the phonon bath associated with the specific protein and can be approximated by log-normal distribution function as

$$J_{ph}(\omega) = \frac{1}{\omega\sqrt{2\pi}} \sum_k \frac{S_k}{\sigma_k} \exp\left(-\ln\left(\frac{\omega}{\omega_k^c}\right)^2 / 2\sigma_k^2\right). \tag{41}$$

Values of such function like standard deviation σ_k, cut-off frequency ω_k^c and Huang–Rhys factor S_k are taken from experimental results [22] and given in Table (3). Spectral density function directly relates to coupling strengths g, from the Eq. (6), in the following form

$$g_p^2 = \frac{\Delta}{\pi} J_{ph}(\omega_p), \tag{42}$$

3 Table. WSCP spectral density function parameters.

k	1	2	3	4
σ_k	0.4	0.2	0.2	0.4
ω_k^c	28	54	90	145
S_k	0.45	0.15	0.21	0.15

4 Table. WSCP internal vibrational mode parameters.

Mode	1	2	3	4	5	6	7	8
w_j	93	189	262	352	389	519	573	745
S_j	0.012	0.010	0.013	0.023	0.015	0.016	0.017	0.034

where Δ is the discretization frequency step. Then the coupling strengths are normalized using reorganization energy Λ^{ph}, defined as

$$\Lambda^{ph} = \sum_p g_p^2 \omega_p. \tag{43}$$

The value used in this work is $\Lambda^{ph} = 65$ cm^{-1} [23] together with 100 local phonon modes and frequencies $\omega = 1 \ldots 500$ cm^{-1}.

Regarding intramolecular vibrational modes, we used specific values for frequency w_j and Huang–Rhys factor S_j that were taken from [25] and are presented in Table (4). In this case, a coupling strengths f in the Eq. (8), has a straightforward relationship to Huang–Rhys factor, given by $f_j = \sqrt{S_j}$. For simplicity, we only included 8 modes with highest Huang–Rhys factors and frequencies up to $w_j = 750$ cm^{-1}, because higher frequency modes do not significantly contribute to the main excitonic peak and therefore can be omitted.
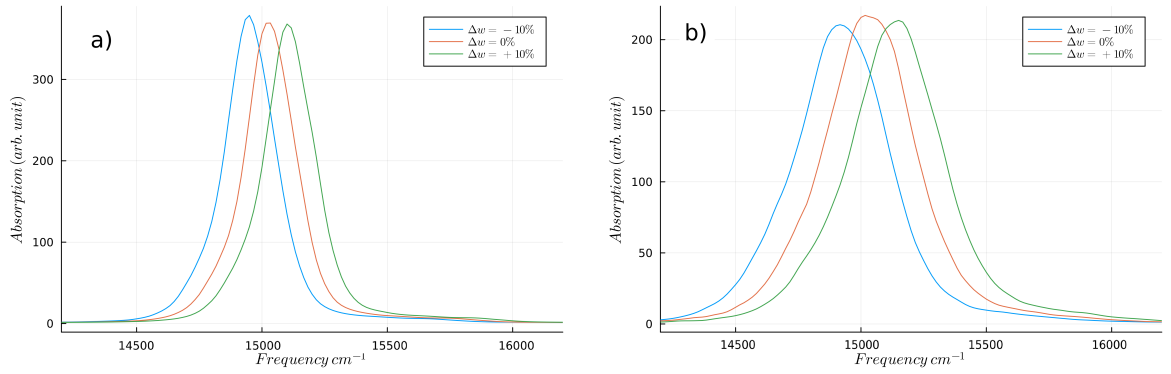
3.2 Absorption spectra

First of all, we start our analysis by investigating the absorption spectra of our system model. Fig. (5) compares experimentally obtained spectra [4] with our calculated ones at two temperatures temperature, $4.5K$ and $300K$. It needs to be noted here that at this point the nonlinear effect is not included and in turn no squeezing of bath vibrational modes takes place. We see that experimental spectra at $4.5K$ exhibit two exciton peaks at around 14900 cm^{-1} and 15150 cm^{-1}, this is because WSCP aggregate forms two weakly coupled dimers [3], each producing aforementioned peaks. The higher frequency range is dominated by internal vibrational modes. When comparing the experimental spectra with our results in Fig. (5a), we observe a good alignment of the main peak at 15150 cm^{-1}. However, we do not observe the lower frequency excitonic peak at 14900 cm^{-1} and the vibrational progression in higher frequencies ranging from around 15500 cm^{-1} to 17000 cm^{-1}. The former discrepancy could be attributed to the TDVP approach producing only an approximation rather than an exact solution. The latter discrepancy could be due to the coupling of the system to internal vibrational modes, being too small in our model.

Next, we investigate how nonlinearity impacts the absorption spectrum. We do that by chang-
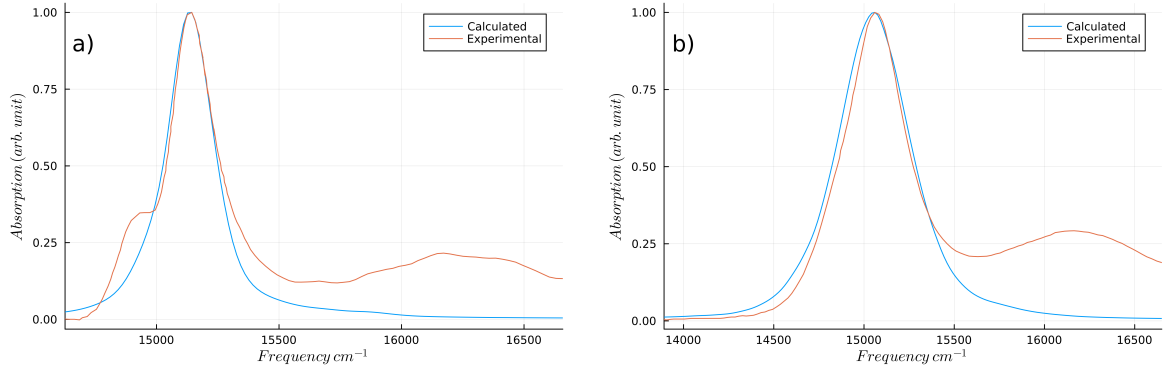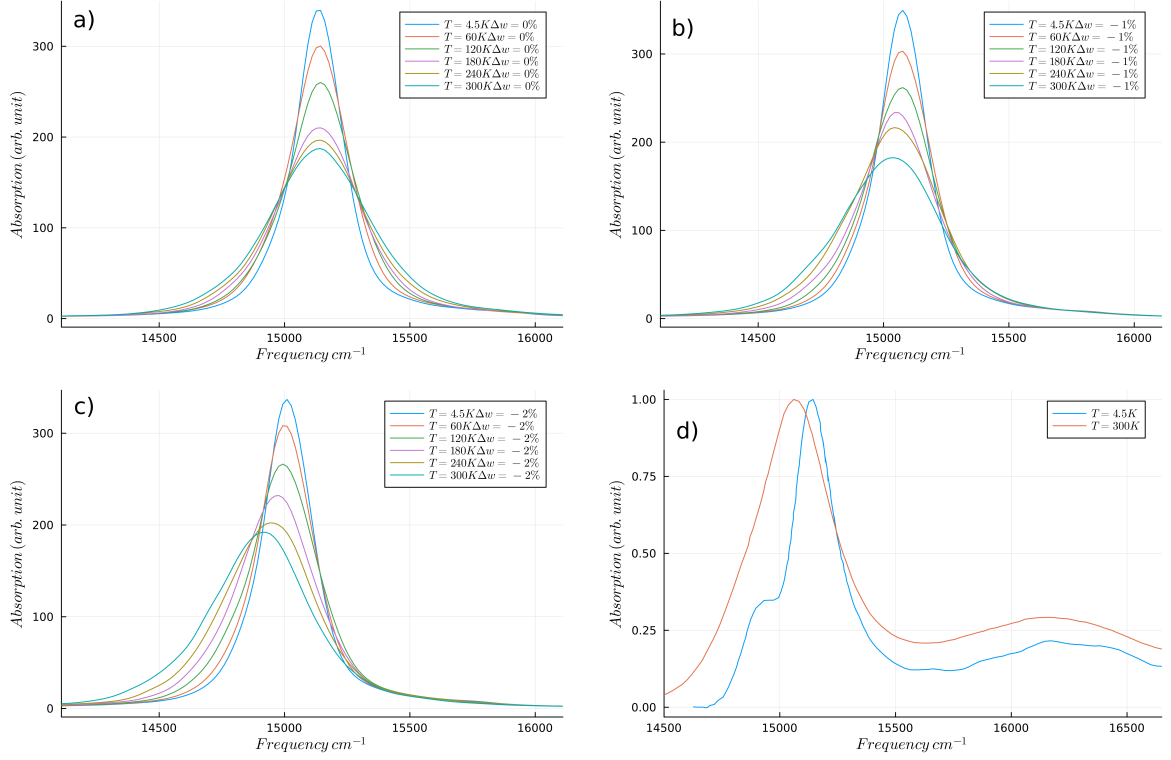
5 Fig. Calculated WSCP absorption spectra compared with experimentally obtained ones a) $T = 4.5K$ and at b) $T = 300K$

6 Fig. Calculated absorption spectra with different vibrational mode frequency difference $\Delta\omega$ at a) $T = 4.5K$ and at b) $T = 300K$

ing two parameters: bath vibrational mode frequency difference $\Delta\omega$ from -10% to 10% and then temperature T from $4.5K$ to $300K$. The results can be seen in Fig. (6). What we see here is that at $T = 4.5K$, by increasing $\Delta\omega$ the whole spectrum shifts to the right (to a higher frequency range) and vice versa. One more thing to note is that with the increase in vibrational mode frequency difference, the peak height decreases slightly, and this could be due to the fact that the gap between vibrational mode peaks increases, which somewhat contributes to the excitonic main peak, in turn broadening the whole spectrum. At $T = 300K$ we see same pattern, except the peak pattern downwards cannot be noticed.

The next thing we do is to compare if squeezing has different effects at different temperatures. In Fig. (7a) we can see the spectra distribution when there is no frequency difference at different temperatures from $4.5K \ldots 300K$. We observe that with the increase in temperature spectra leads to broader peaks. Now if we try to include frequency difference together with temperature increase we observe quite a clear phenomena where the spectra start to shift to the lower frequency range as shown in Fig. (7b) and Fig. (7c). This could be due to the fact that by adding nonlinear interaction and squeezing effect, we are making an excited state energy potential shallower and increased temperatures introduces stochastic fluctuations in the energy levels ground and excited states, in turn shifting spectrum to lower energies. This is a promising result because, according to experimentally obtained data [3], the temperature shift was also observed. At the $T = 77K$ spectrum exhibits

7 Fig. Calculated absorption spectra progression at different temperatures when there is no vibrational mode frequency difference (a) shows no main peak shift. (b) With 1% frequency difference and (c) 2% frequency difference shows clear shift to the lower energy region. (d) Experimentally obtained spectra at two different temperatures also shows frequency shift [3].

narrower peaks and a slight blue shift by about 77 cm^{-1} as compared to the room temperature $T = 300K$ absorption spectrum as show in Fig. (7d). This fits quite well with our results, because according to our calculations, a 2% in frequency difference results in a similar absorption spectrum shift at about 83 cm^{-1}.

3.3 2D spectra

3.3.1 Comparison with experimental data

Now, let's look at the equivalent 2D WSCP spectra. To get this kind of spectra it requires double excitation of our system model with ground state g, single excited state e, and a double excited state f, therefore we can use the full form of our equations that we derived in Eq. (32 - 36). Calculated 2DES spectrum together with experimental spectra [3] is shown in Fig. (8). For calculations we use waiting time is $t_2 = 60$ fs, temperature $T = 77K$, vibrational mode frequency difference $\Delta\omega = -2\%$ (one that we established in the previous subsection) while keeping all other parameters the same as in the previous 1D spectra calculations. The reason for choosing these specific waiting time and temperature values is that they represent the lowest values observed in experimental data, thereby minimizing environmental and relaxation effects. If we compare the two spectra we see that they share a significant similarity in that they both have a single central peak along the diagonal at $\omega_1 = \omega_3 = 15175$ cm^{-1}, which indicates that they are dominated by GSB and ESE signals. The main
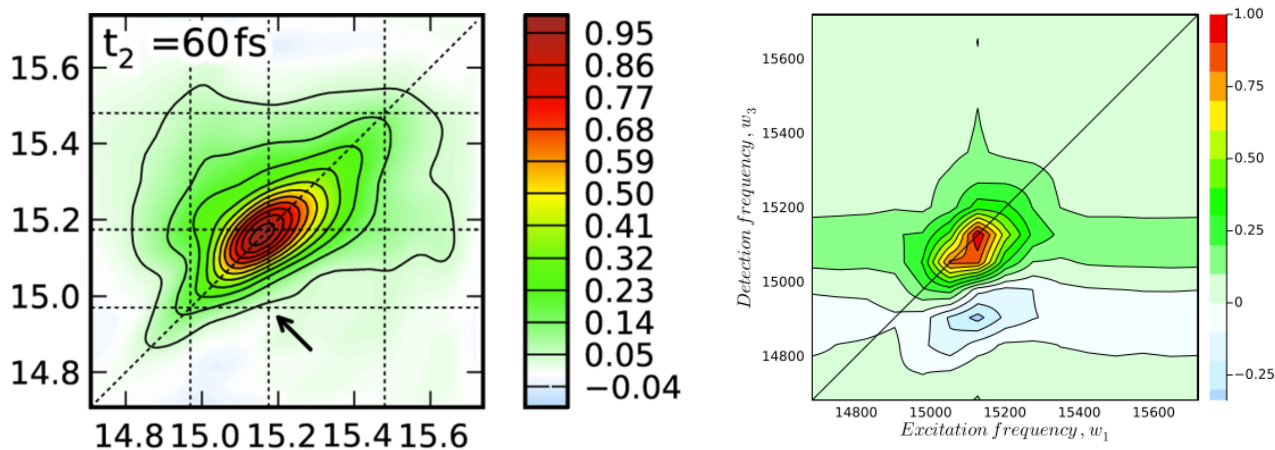
8 Fig. Experimental left and calculated right 2D spectra at $t_2 = 60$ fs, $T = 77K$ and $\sigma = 70$ cm^{-1}.

peak is also much more elongated, or broader, along the diagonal in the experimental spectrum. Just below the diagonal at around $\omega_1 = 15175$ cm^{-1} and $\omega_3 = 14970$ cm^{-1}, a prominent negative cross-peak can be seen in both spectra, although in calculated spectra it is much more visible. This peak represents ESA signal which indicates that the energy difference between states f and e (ω_{fe}) is lower compared with energy level between e and g (ω_{eg}).

3.3.2 Tuning static disorder value

As it was mentioned before, the experimental spectrum exhibits an increase in the width along the diagonal, which is not seen in our calculated spectra. This kind of effect is called inhomogeneous broadening which provides insights into the interactions between the system and its environment. When a system consists of a number of identical molecules, each interacts with the environment differently, resulting in small variations in the same electronic state of each molecule. On the other hand, homogeneous broadening occurs when the spectrum is broadened along off-diagonal and is due to interactions between the molecules in the system which cause all of the molecules to experience similar broadening. The ability to distinguish between homogeneous and inhomogeneous broadening is one of the benefits of 2D spectroscopy.

Inhomogeneous broadening can arise from static disorder, which we can directly control by changing the value of Gaussian functions standard deviation σ [21]. The results of 2D spectra with different static disorder values ranging from 70 cm^{-1} to 200 cm^{-1} can be seen in Fig. (9). Here we see that the disorder does affect our system's inhomogeneous broadening. Comparing results with experimental data in Fig. (8) we see that the best alignment is with Fig. (9 c) representing $\sigma = 150$ cm^{-1} value. Increasing static disorder over more, the spectrum becomes too broad and starts to lose its structure. Therefore, for the subsequent calculation we used the aforementioned value.
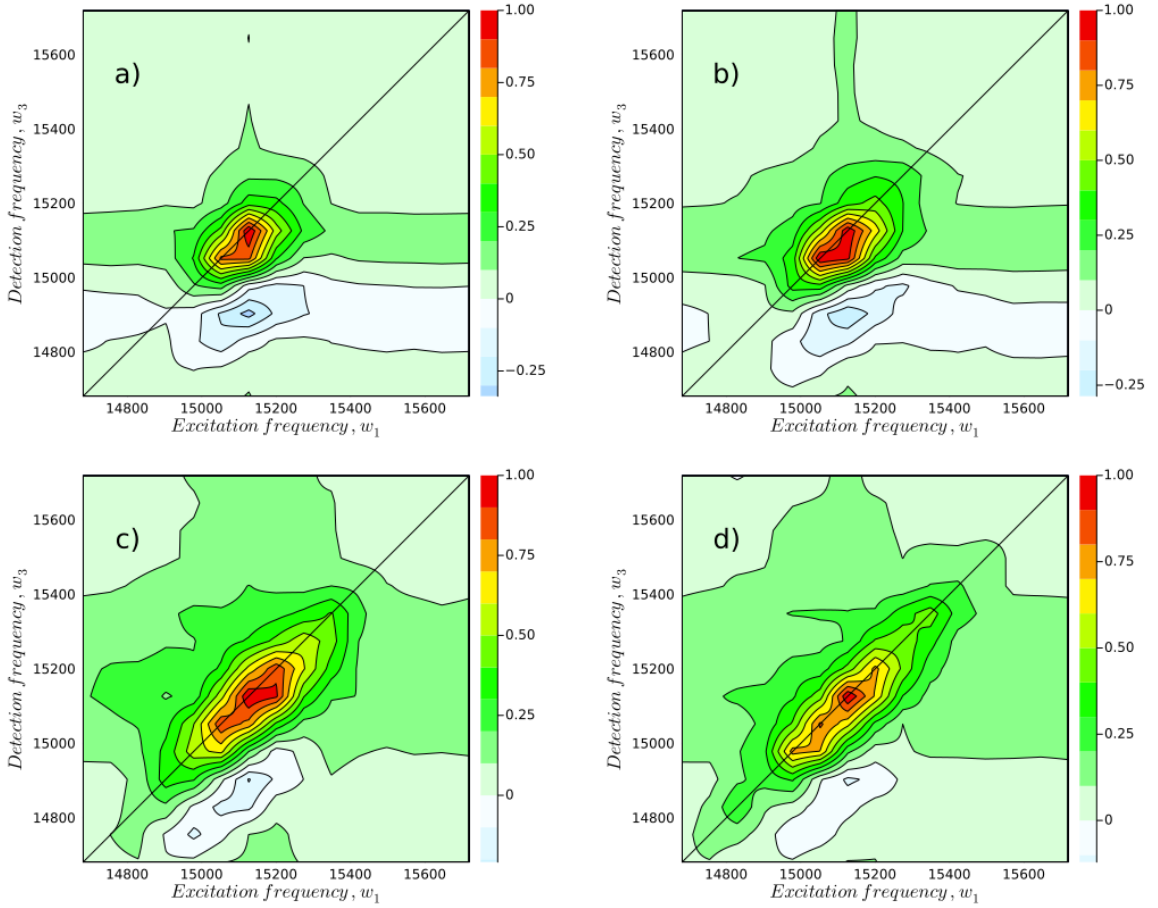
9 Fig. Calculated 2D spectra at $t_2 = 60$ fs and $T = 77K$, but with different static disorder values a) $\sigma = 70$ cm^{-1}, b) $\sigma = 100$ cm^{-1}, c) $\sigma = 150$ cm^{-1}, d) $\sigma = 200$ cm^{-1}.
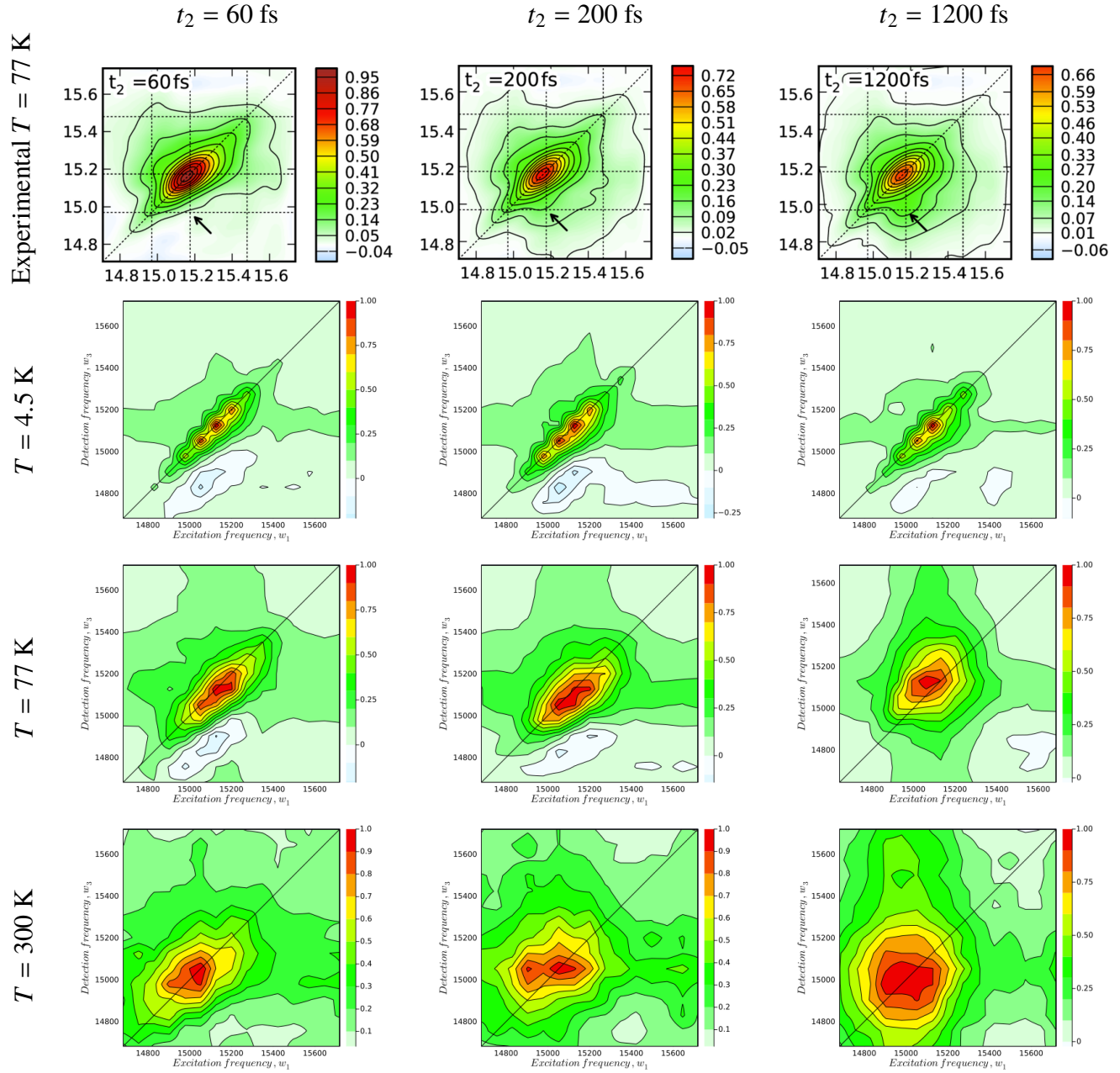
3.3.3 Spectra at different waiting times and temperatures

Once we have established required parameters, namely frequency difference and static disorder, we investigate our system by varying the waiting time t_2. The experimental and calculated spectra are organized in a grid in Fig. (10), with columns representing different waiting times $t_2 = [60$ fs$, 200$ fs$, 1200$ fs$]$ and rows representing different temperatures $T = [4.5$ K$, 77$ K$, 300$ K$]$. We chose the 4.5 K temperature because it is close to absolute zero which eliminates any temperature effects, 77 K temperature because it is the only temperature that the experimental data is available for, and 300 K represents room temperature.

As we compare the calculated results at 77 K with the experimental data, we observe a decrease in spectral distinctness and an overall increase in spectral diffusion in all directions as the waiting time increases. This can be attributed to the increased time available for the excited state population to evolve and undergo various relaxation pathways. Another thing to note is that in the experimental spectrum, the negative ESA peak is discernible only at $t_2 = 60$ fs, after which it merges with the main peak and becomes indistinguishable. In contrast, the calculated spectra display a visible ESA peak even at $t_2 = 200$ fs. Overall alignment with experimental data is quite good.

Now if we look at 4.5 K temperature spectra, four distinct peaks can be seen, each representing a distinct excitons in our system model. However, at higher temperatures, these peaks fuse together

which leads to a loss of spectral resolution. This is because at higher temperatures, the excited state lifetime becomes shorter due to a broader distribution of energies, which leads to relaxation processes, resulting in broader spectral lines. Another thing to mention here is that we also observe that there is a shift of diagonal peak to a lower frequency range with the increase in temperature, similar to what is observed in absorption spectra calculations.

10 Fig. Calculated and experimental 2D spectra. Columns represent different waiting times $t_2 = [60\text{ fs}, 200\text{ fs}, 1200\text{ fs}]$ and rows represent different temperatures $T = [4.5\text{ K}, 77\text{ K}, 300\text{ K}]$. Experimental spectra were measured at $T = 77$ K.

4 Conclusions

1. When considering quadratic electron-vibration coupling, it becomes necessary to use a more accurate representation of the wave function, such as the squeezed coherent state.

2. The experimental WSCP absorption spectrum shows a blue shift when the temperature is lowered to 77 K compared to the absorption spectrum at room temperature. To replicate this effect, it is necessary to include squeezed coherent states in a trial wavefunction and quadratic coupling effect with 2% in frequency difference.

3. 2DES spectrum allows to fine-tune static disorder parameter, which at 77 K was estimated to be $150 \, \text{cm}^{-1}$.

4. Our calculations on WSCP 2DES spectrum reveal four distinct excitonic peaks only at 4.5 K temperature.

5. The dynamics of our model accurately capture the experimental 2DES when we vary the waiting time. This indicates that the interaction with phonons is properly accounted for in our model.

References

[1] Y. V. Maleeva, K. V. Neverov, Y. N. Obukhov, and M. S. Kritsky, Water Soluble Chlorophyll-Binding Proteins of Plants: Structure, Properties and Functions., *Molekuliarnaia biologiia*, 2019, **53**, 998–1011.

[2] G. Renger, J. Pieper, C. Theiss, *et al.*, Water soluble chlorophyll binding protein of higher plants: A most suitable model system for basic analyses of pigment–pigment and pigment–protein interactions in chlorophyll protein complexes, *Journal of Plant Physiology*, aug 2011, **168**, 1462–1472.

[3] J. Alster, H. Lokstein, J. Dostál, A. Uchida, and D. Zigmantas, 2D Spectroscopy Study of Water-Soluble Chlorophyll-Binding Protein from Lepidium virginicum, *The Journal of Physical Chemistry B*, apr 2014, **118**, 3524–3531.

[4] A. Kell, D. Bednarczyk, K. Acharya, J. Chen, D. Noy, and R. Jankowiak, New Insight into the Water-Soluble Chlorophyll-Binding Protein from Lepidium virginicum, *Photochemistry and Photobiology*, may 2016, **92**, 428–435.

[5] D. Horigome, H. Satoh, N. Itoh, K. Mitsunaga, I. Oonishi, A. Nakagawa, and A. Uchida, Structural Mechanism and Photoprotective Function of Water-soluble Chlorophyll-binding Protein, *Journal of Biological Chemistry*, mar 2007, **282**, 6525–6531.

[6] D. Bednarczyk, S. Takahashi, H. Satoh, and D. Noy, Assembly of water-soluble chlorophyll-binding proteins with native hydrophobic chlorophylls in water-in-oil emulsions, *Biochimica et Biophysica Acta (BBA) - Bioenergetics*, 2015, **1847**, 307–313.

[7] R. Loudon, *The Quantum Theory of Light*. Oxford science publications, OUP Oxford, 2000.

[8] N. Zhou, L. Chen, Z. Huang, K. Sun, Y. Tanimura, and Y. Zhao, Fast, Accurate Simulation of Polaron Dynamics and Multidimensional Spectroscopy by Multiple Davydov Trial States, *The Journal of Physical Chemistry A*, mar 2016, **120**, 1562–1576.

[9] D. Abramavičius and T. Marčiulionis, Excitation dynamics of two level quantum systems coupled to Morse vibrations, *Lithuanian Journal of Physics*, jan 2019, **58**.

[10] M. Jakučionis, A. Žukas, and D. Abramavičius, Inspecting molecular aggregate quadratic vibronic coupling effects using squeezed coherent states, *Physical Chemistry Chemical Physics*, 2023, **25**, 1705–1716.

[11] L. Valkunas, D. Abramavicius, and T. Mancal, *Molecular Excitation Dynamics and Relaxation*. 2013.

[12] J. Jiang, D. Abramavicius, C. Falvo, B. M. Bulheller, J. D. Hirst, and S. Mukamel, Simulation of Two-Dimensional Ultraviolet Spectroscopy of Amyloid Fibrils, *The Journal of Physical Chemistry B*, sep 2010, **114**, 12150–12156.

[13] A. Gelzinis, R. Augulis, V. Butkus, B. Robert, and L. Valkunas, Two-dimensional spectroscopy for non-specialists, *Biochimica et Biophysica Acta (BBA) - Bioenergetics*, 2019, **1860**, 271–285.

[14] R. V. G. Leonas Valkunas, Herbert Van Amerongen, *Photosynthetic Excitons*. 2000.

[15] V. Chorošajev, A. Gelzinis, L. Valkunas, and D. Abramavicius, Dynamics of exciton-polaron transition in molecular assemblies: The variational approach, *The Journal of Chemical Physics*, jun 2014, **140**, 244108.

[16] T. D. Huynh, K.-W. Sun, M. Gelin, and Y. Zhao, Polaron dynamics in two-dimensional photon-echo spectroscopy of molecular rings., *The Journal of chemical physics*, sep 2013, **139**, 104103.

[17] L. Chen, M. F. Gelin, W. Domcke, and Y. Zhao, Theory of femtosecond coherent double-pump single-molecule spectroscopy: Application to light harvesting complexes., *The Journal of chemical physics*, apr 2015, **142**, 164106.

[18] L. Chen, M. F. Gelin, and W. Domcke, Multimode quantum dynamics with multiple Davydov D 2 trial states: Application to a 24-dimensional conical intersection model, *The Journal of Chemical Physics*, jan 2019, **150**, 024101.

[19] S.S. Mukamel, *Principles of Nonlinear Optical Spectroscopy*. New York: Oxford University Press, 1995.

[20] V. Chorošajev, T. Marčiulionis, and D. Abramavicius, Temporal dynamics of excitonic states with nonlinear electron-vibrational coupling, *The Journal of Chemical Physics*, aug 2017, **147**, 074114.

[21] O. Rancova, R. Jankowiak, and D. Abramavicius, Probing environment fluctuations by two-dimensional electronic spectroscopy of molecular systems at temperatures below 5 K, *The Journal of Chemical Physics*, 2015, **142**.

[22] A. Kell, X. Feng, M. Reppert, and R. Jankowiak, On the Shape of the Phonon Spectral Density in Photosynthetic Complexes, *The Journal of Physical Chemistry B*, jun 2013, **117**, 7317–7323.

[23] M. Jakučionis, V. Chorošajev, and D. Abramavičius, Vibrational damping effects on electronic energy relaxation in molecular aggregates, *Chemical Physics*, nov 2018, **515**, 193–202.

[24] O. Rancova, R. Jankowiak, A. Kell, M. Jassas, and D. Abramavicius, Band Structure of the Rhodobacter sphaeroides Photosynthetic Reaction Center from Low-Temperature Absorption and Hole-Burned Spectra, *The Journal of Physical Chemistry B*, jun 2016, **120**, 5601–5616.

[25] A. Gelzinis, D. Abramavicius, J. P. Ogilvie, and L. Valkunas, Spectroscopic properties of photosystem II reaction center revisited, *The Journal of Chemical Physics*, 2017, **147**.

VANDENYJE TIRPAUS CHLOROFILŲ KOMPLEKSO (WSCP) NETIESINIŲ SPEKTRŲ MODELIAVIMAS

Agnius Žukas

Santrauka

Fotosintezės metu kompleksai, sudaryti iš pigmentų ir baltymų, surenka saulės šviesos energiją specializuotose šviesos surinkimo antenose ir tiekia energiją reakcijos centrams, kur sužadinimo energija naudojama krūviams atskirti. Vandenyje tirpus chlorofilą surišantis baltymas (WSCP) yra vienas iš tų visur esančių fotosintetinių molekulinių agregatų, randamų gamtoje. Tokios sistemos pasižymi sudėtinga kvantine sužadinimo dinamika ir paprastai modeliuojamos naudojant Frenkelio eksitono modelį, susietą su virpesinėmis modomis, vaizduojančiomis aplinką.

Šiame darbe kvantinei sužadinimo dinamikai aprašyti taikome nuo laiko priklausantį variacinį metodą (angl. Time-Dependent Variational Principle). Šio metodo tikslumas labai priklauso nuo pasirinktos banginės funkcijos, dėl šios priežasties panaudojome suspaustą paslinktą koherentinių būsenų bazę. Aprašydami sistemos modelį taip pat įtraukiame papildomą netiesinę kvadratinę sąveiką tarp elektroninių sužadinimų ir virpesinių modų. Pastaroji sąveika leidžia priskirti skirtingus virpesinių modų dažnius pagrindinėje ir sužadintoje būsenose, kurių skirtumas tiesiogiai įtakoja koherentinės būsenos suspaudimą.

Norint visapusiškai ištirti fotosintezės pigmento-baltymų agregatų sužadinimo dinamiką, eksperimentiškai ir teoriškai turi būti naudojami įvairūs spektroskopiniai metodai. Vienas paprasčiausių - tiesinė sugerties spektroskopija, o pažangesnė technika - vadinama dvimate elektronine spektroskopija (angl. Two-Dimensional Electronic Spectroscopy). Norėdami pamatyti, kaip netiesinė sąveika ir suspausta koherentinė būsenų bazė paveikia sistemos dinamiką, apskaičiuojame sugerties ir dvimatį spektrus.

Įsitikinome, kad tyrinėjant kvadratinę sąveiką tarp elektroninių sužadinimų ir virpesinių modų yra būtina naudoti tikslesnį banginės funkcijos atvaizdavimą, pvz., suspaustą koherentinę būseną. Sugebėjome atkartoti WSCP sugerties spektro poslinkį į žemesnių dažnių diapazoną, kai temperatūra yra didinama. Šį eksperimentuose atrastą efektą galima atkartoti tik su suspausta koherentine būsena, tam reikalingas 2% dažnių skirtumas tarp pagrindinės ir sužadintos būsenos. Taip pat apskaičiavome dvimatį WSCP spektrą ir nustatėme geriausią statinės netvarkos parametro reikšmę, kuri ties 77 K temperatūra yra 150 cm^{-1}. Palyginome eksperimentinius ir suskaičiuotus spektrus su skirtingais laukimo laikais ir temperatūromis. Pamatėme, kad ties 4.5 K temperatūra spektre ant diagonalės atsiranda keturios aiškiai atskirtos smailės, kurių nematyti nei eksperimentiniuose, nei suskaičiuotuose spektruose ties 77 K temperatūra. Keičiant laukimo laiką, mūsų modelio dinamika pakankamai tiksliai atitinka eksperimentinius spektrus. Tai rodo, kad taikytame modelyje tinkamai atsižvelgta į sąveiką su fononais.